

Low swirl premixed methane-air flame dynamics under acoustic excitations

Cite as: Phys. Fluids **31**, 095106 (2019); <https://doi.org/10.1063/1.5118826>

Submitted: 06 July 2019 . Accepted: 27 August 2019 . Published Online: 17 September 2019

M. Shamsavari, M. Farshchi, S. R. Chakravarthy, A. Chakraborty, I. B. Aravind, and B. Wang (王兵)



View Online



Export Citation



CrossMark

ARTICLES YOU MAY BE INTERESTED IN

[Drag reduction in turbulent flow along a cylinder by circumferential oscillating Lorentz force](#)

Physics of Fluids **31**, 095104 (2019); <https://doi.org/10.1063/1.5118699>

[Three-dimensional simulation of a rising bubble in the presence of spherical obstacles by the immersed boundary-lattice Boltzmann method](#)

Physics of Fluids **31**, 097104 (2019); <https://doi.org/10.1063/1.5115097>

[Front dynamics in exchange flow of two immiscible iso-viscous fluids in two-dimensional straight and curved plane channels](#)

Physics of Fluids **31**, 092105 (2019); <https://doi.org/10.1063/1.5108748>

Scilight

Highlights of the best new research
in the physical sciences

LEARN MORE!



Low swirl premixed methane-air flame dynamics under acoustic excitations

Cite as: *Phys. Fluids* **31**, 095106 (2019); doi: [10.1063/1.5118826](https://doi.org/10.1063/1.5118826)

Submitted: 6 July 2019 • Accepted: 27 August 2019 •

Published Online: 17 September 2019



M. Shahsavari,^{1,2,a)} M. Farshchi,¹ S. R. Chakravarthy,³ A. Chakraborty,³ I. B. Aravind,³ and B. Wang (王兵)²

AFFILIATIONS

¹Department of Aerospace Engineering, Sharif University of Technology, Tehran 1458889694, Iran

²School of Aerospace Engineering, Tsinghua University, Beijing 100084, China

³Department of Aerospace Engineering, and National Centre for Combustion Research and Development, Indian Institute of Technology Madras, Chennai 600036, India

^{a)} Author to whom correspondence should be addressed: shahsavari@ae.sharif.ir and shahsavari@mail.tsinghua.edu.cn.
Tel.: +86-15510027703.

ABSTRACT

In this study, simultaneous particle image velocimetry and planar laser induced fluorescence of hydroxyl radical, chemiluminescence imaging, and hot-wire measurements are utilized to study reacting low swirl flow dynamics under low to high amplitude acoustic excitations. Results show that a temporal weak recirculation zone exists downstream of the flame, which is enlarged in size under acoustic excitations. Investigations show that temporal behaviors of this recirculation zone play a significant role in flame movements and instabilities. As the acoustic wave amplitude increases, the flame lift-off distance changes drastically, resulting in flame instabilities (flashback and blowout) during the excitations. Prior to the flame blowout, although the flame lift-off distance responds periodically to the acoustic perturbations, heat release fluctuations display an aperiodic response. Flame dynamics are further studied by calculated power spectra of acoustic velocity and heat release fluctuations and reconstructed phase portraits of heat release fluctuations. Investigations show that increasing the forcing amplitude results in more deterministic features in the flame dynamics and amplification of the higher harmonic modes in the heat release fluctuations. However, such regular patterns become scattered prior to the flame blowout due to the existence of nonlinearities induced by high amplitude excitations. It is speculated that flame blowout can be a symptom of such nonlinearities. The Rayleigh index is measured to study thermoacoustic couplings. At low amplitude excitations, various coupling patterns occur at the flame. However, such complex patterns are replaced by simple coherent patterns, when the flame is excited by high amplitude acoustic perturbations.

Published under license by AIP Publishing. <https://doi.org/10.1063/1.5118826>

I. INTRODUCTION

Low nitrogen oxides (NO_x) combustion devices are highly relevant to meet increasingly stringent emission regulations. Lean premixed low swirl combustion is one of the novel technologies to reduce NO_x emissions.¹ The most important benefit of utilizing low swirl technology as compared to other lean premixed methods, viz., high swirl technology, is that in low swirl technology, the premixed flame is stabilized aerodynamically without any recirculating flow motion.^{2,3} The lack of strong recirculation zones (RZs) in low swirl flows decreases the residence time of the combustion products in high temperature zone, which in turn reduces NO_x emissions.⁴ Unfortunately, it is well known that lean premixed combustion is highly susceptible to thermoacoustic instabilities.⁵

Despite valuable concerted community efforts aimed at understanding combustion instabilities, predicting combustion instabilities and the key physical processes controlling the instabilities have been the subjects of growing attention to prevent or tackle catastrophic problems caused by combustion instabilities in combustors.⁵⁻⁹ Such instabilities are compounded in low swirl combustion by the fact that low swirl flames are stabilized aerodynamically at relatively considerable distances downstream of the burner rim. Low swirl flame stabilization mechanism makes the flame more prone to both vortical and acoustic perturbations, which can increase the likelihood of combustion instabilities.¹⁰ Therefore, identification of low swirl flame dynamic response to acoustic excitations is imperative to make low swirl burners industrially applicable. To such aim, it is usually preferable to study flame response in

an unconfined configuration under external harmonic forcing perturbations.¹¹

Kang *et al.*¹² and Huang and Ratner¹³ used planar laser induced fluorescence of hydroxyl radical (OH-PLIF) and pressure measurements to evaluate a low swirl flame response and the corresponding Rayleigh criteria. Based on Rayleigh index patterns, it was found that there is a thermoacoustic coupling at the shear layer near the boundary of the low swirl flame under acoustic excitations. The coupling is believed to be a result of shear layer entrainments at the flame boundaries.^{12,14} Yilmaz *et al.* determined effects of hydrogen addition on methane-air low swirl flame response.¹⁵ They reported that hydrogen addition increases the thermoacoustic coupling. Davis *et al.* used excited hydroxyl radical (OH*) chemiluminescence and phase-locked particle image velocimetry (PIV) to study self-excited oscillations of a model combustor utilizing a low swirl burner.¹⁶ Investigations were carried out on two flames; a methane-air flame and a methane/hydrogen-air flame. Obtained results showed that the methane/hydrogen blended flame is attached to the burner, while the methane flame is lifted. Results corroborated the main findings of the previous investigations by showing that thermoacoustic couplings increase by hydrogen addition. Ranalli and Ferguson investigated effects of the exhaust gas recirculation on a low swirl flame transfer function using chemiluminescence measurements.¹⁷ They showed that exhaust gas recirculation has no considerable effect on the flame transfer function.¹⁷ Zhang and Ratner studied effects of the elevated pressure on a low swirl flame response.¹⁸ Results showed that at high enough pressure and fluctuation levels, elevated pressure intensifies the pressure fluctuations, if heat release fluctuations are in phase with pressure fluctuations. Bagheri-Sadeghi *et al.* studied effects of acoustic perturbations on low swirl flames using high-speed imaging.¹⁹ Obtained results showed that there are considerable thermoacoustic couplings at the boundary of the low swirl flame, which are believed to be the result of flame-turbulent flow interactions at the shear layers.¹⁹ In addition to the above

experimental investigations, Shahsavari *et al.* utilized large eddy simulations to examine effects of the external excitations on reacting low swirl flow characteristics.^{14,20} Numerical investigations showed that external excitations increase the local swirl number upstream of the flame front. Such increases in the swirl number is at maximum value, when the flow is excited at the dominant hydrodynamic frequency of the flow field, which in turn induces a central recirculation zone.²⁰

The main objective of the present study is to increase our understanding of reacting low swirl flow dynamics under acoustic excitations, in particular, the influence of acoustic wave amplitudes on the flow and flame dynamics. To such aim, simultaneous PIV and OH-PLIF methods along with OH* chemiluminescence and hot wire measurements are utilized to capture detailed aspects of low swirl flow and flame dynamics under acoustic excitations. The present investigation is organized as follows. Section II of the paper describes the experimental configuration. Section III presents results and discussions. Section IV concludes the paper.

II. EXPERIMENTAL CONFIGURATION

The experimental setup used in the present study is schematically shown in Fig. 1. The experiments are performed using a methane-air mixture (with equivalence ratio of 0.62). Compressed air is supplied from a 10 bars compressor facility. Furthermore, research grade methane (99.5% pure) is used for the present investigations. Air and fuel are perfectly premixed in a tube of 1000 mm length and 19 mm diameter upstream of the settling chamber. The air and fuel flow rates are measured using laminar flow elements (with the accuracy of 0.2% of the full scale). The premixed air and fuel mixture is sent from the bottom of the settling chamber. In order to straighten the flow, a honeycomb section with cell size of 5 mm is used at the bottom of the settling chamber. Further downstream of the honeycomb section, 5 layers of mesh screens with size of 1 mm² are used to remove large scale turbulence structures. A

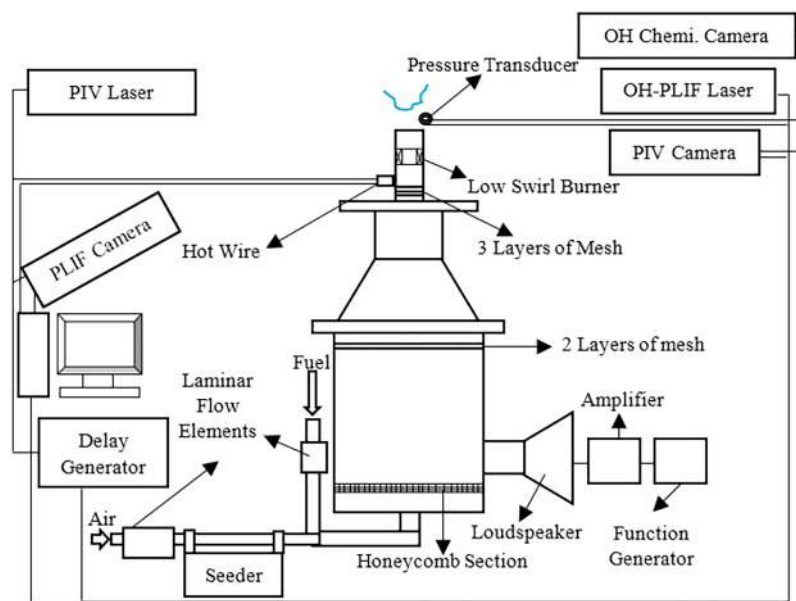


FIG. 1. Schematic of the experimental setup.

vane type low swirl burner used in this investigation is designed based upon the design rules proposed by Cheng *et al.*^{21,22} The geometry of the low swirl burner employed in the present study has been described in detail in our previous papers.^{10,19} However, a concise description is presented here for completeness. The low swirl burner consists of two sections; center channel and swirl annulus. The inner diameter of the burner and center channel are 40 mm and 28 mm, respectively. The center channel screen has 29 holes of 2.5 mm diameter. The swirler annulus consisted of 9 curved vanes with discharge angle of 37° , which are attached to the center channel. The burner swirl number is 0.5, which is defined as the axial flux of the angular momentum divided by the axial flux of the axial momentum and the burner diameter.²²

In order to excite the low swirl flame, a function generator is used to generate harmonic signals. Then, the signals are amplified by an amplifier and are supplied to a loudspeaker placed in the settling chamber. In this paper, high speed OH* chemiluminescence imaging is employed to characterize the transient low swirl flame dynamics under external acoustic excitations. This method uses a high-speed camera with resolution of 1280×800 and frame rate of 7000 Hz. The camera is fitted with an intensifier, a 105 mm ultraviolet (UV) lens and a hydroxyl (OH) filter (310 ± 10 nm). Typically, 9000 images are used to calculate the ensemble averaged results. Moreover, in order to collect the pressure and velocity data a piezo pressure transducer and a hot wire are mounted at the burner outlet and swirler inlet, respectively. The hot wire relative expanded uncertainty comprising of calibrator, linearization related to the curve fitting and ambient temperature and pressure deviations is 3% with a 95% confident interval. Moreover, the piezo pressure transducer relative uncertainty is 2.5%.

In the present study, simultaneous PIV and OH-PLIF measurements are used to obtain velocity and relative OH distributions to study various features of the unexcited and excited low swirl flames. To such aim, two separate systems are used for PIV and OH-PLIF aligned on opposite sides to illuminate a planar region of the reacting flow. Pixel matching is carried out for cameras and the fields-of-view overlapped; the resolution is kept the same across both cameras used for PIV and OH-PLIF measurements. The selected plane crosses the vertical centerline of the low swirl burner. Figure 2 shows the temporal separation of PIV and OH-PLIF laser pulses. In the excited case, both PIV and OH-PLIF techniques are applied in a

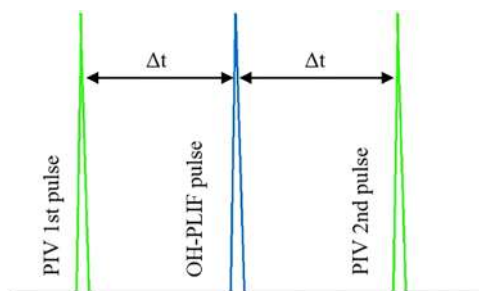


FIG. 2. Temporal separation of PIV and OH-PLIF laser pulses.

phase-locked mode. To such aim, the pressure transducer signal was taken as the reference for triggering the phase-locked measurements. Then, PIV, OH-PLIF and signal generator systems are triggered using a delay generator.

The OH-PLIF system consists of (a) an neodymium-doped yttrium aluminum garnet (Nd:YAG) pulsed laser (with 532 nm, 750 mJ/pulse, repetition rate: 10 Hz) to pump a tunable dye laser (with Rhodamine 590 dye with 30 mJ/pulse) to excite OH radicals at $\lambda = 281.8$ nm, (b) a beam steering collimated sheet optic lens ($75 \text{ mm} \times 1 \text{ mm}$), (c) an intensified camera (pixel resolution: 1024×1024 , maximum frame per second 10 fps) fitted with a 50 mm achromatic UV lens and an OH filter (310 ± 10 nm). The laser pulse energy, bandwidth and duration at the measuring location are 1.5 mJ/pulse, 50 1/mm, 200 ns, respectively. Furthermore, the laser light sheet thickness is 1 mm. In the present study, a set of 600 images was recorded to evaluate ensemble averaged OH-PLIF results.

The 2-component PIV system consists of (a) a Nd:YAG laser (pulse energy: 30 mJ/pulse, repetition rate: 10 Hz), (b) a beam steering divergent sheet optic lens ($75 \text{ mm} \times 1 \text{ mm}$), (c) a Sencicam (pixel resolution: 1360×1024 , maximum frame per second 10 fps) fitted with a 50 mm lens and a bandpass filter (532 ± 10 nm). Dry 1–5 μm sized aluminum oxide (Al_2O_3) particles are used to seed the flow. The Stokes drag coefficient for such particles in reacting flows is approximately 0.01.^{23,24} Therefore, the particles follow the flow motions with acceptable accuracy.²⁵ In the present study, the PIV field of view is $93 \text{ mm} \times 116 \text{ mm}$. Furthermore, the PIV interframing time and laser light sheet thickness are chosen to be, respectively, 19 μs and 1 mm to freeze the out of plane motion of the particles. It is well known that PIV measurement bias errors are negligible for a particle image diameter to pixel resolution ratio greater than 4.²⁶ In the present study, the above ratio is 8 and the bias errors are negligible. Another error associated with PIV measurement is the velocity uncertainty. In order to calculate such uncertainty, first, uncertainty of particle displacement should be evaluated. Previous investigations showed that the displacement uncertainty of the particles is usually 5% of the particle diameter.²⁷ Accordingly, in the present study, the velocity uncertainty is 2.6 mm/s based on the displacement uncertainty (0.05 mm) and the PIV interframe time ($\Delta t = 19 \mu\text{s}$). In the present study, a cross correlation algorithm with adaptive multi grid method applied in DaVis 8.3.0 software are used to calculate the velocity field from the recorded images. In the present study, a set of 600 image pairs was recorded to evaluate ensemble averaged velocity results.

III. RESULTS AND DISCUSSIONS

This section is divided into two parts on low swirl flame dynamics. Section III A presents unexcited reacting low swirl flow features using simultaneous PIV and OH-PLIF methods. Next, Sec. III B, discussions are presented on the reacting low swirl flow dynamics under acoustic excitations using OH* chemiluminescence and hotwire anemometry along with simultaneous PIV and OH-PLIF methods.

A. Unexcited low swirl flame

Figures 3(a) and 3(b) show instantaneous distributions of the seeding particles used in PIV measurements and spatial distribution

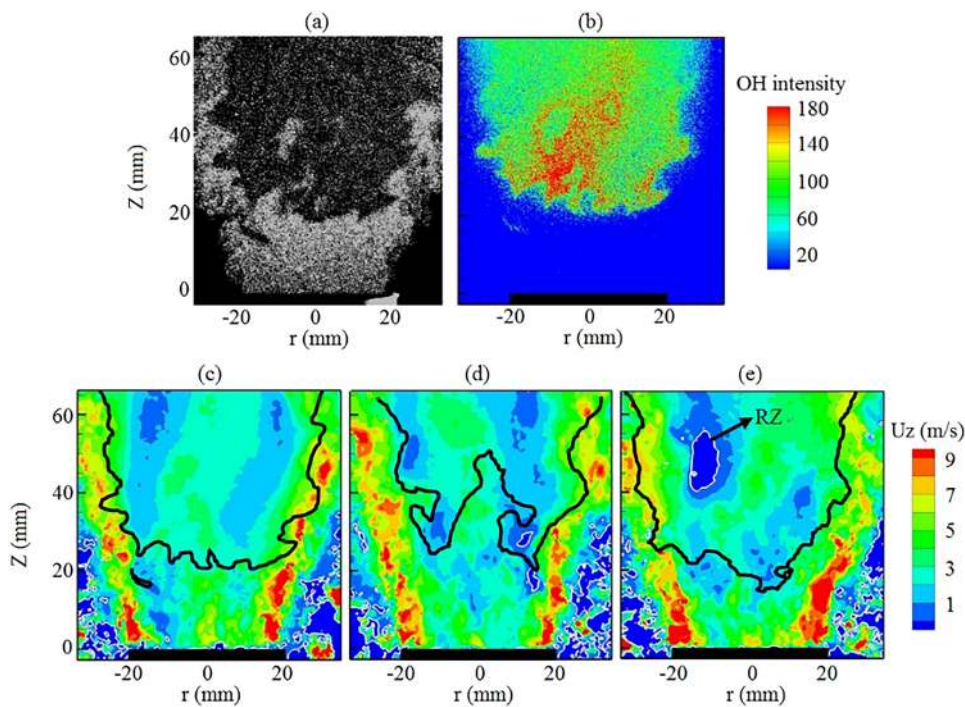


FIG. 3. Instantaneous features of the low swirl flame, (a) scattered laser sheet from the seeding particles, (b) spatial distribution of OH radical from OH-PLIF, and [(c)–(e)] simultaneous axial velocity distribution from PIV and flame boundary (black line) from OH-PLIF.

of OH radical obtained from OH-PLIF in the low swirl flame, respectively. Comparison of these two figures shows that drastic density gradient of the seeding particles is a manifestation of the flame position. In order to study low swirl flame structures and stabilization mechanisms, boundary of the flame is superimposed on the spatial distribution of the axial velocity [Figs. 3(c) and 3(d)]. Here, the flame boundary is marked using OH-PLIF data (at OH intensity = $0.3 \times$ maximum OH intensity). Furthermore, in Figs. 3(c) and 3(d), the white lines show the boundary of regions with negative axial velocity. This criterion is used to discern recirculation zones and vortices. Figures 3(b) and 3(c) show that the low swirl flame is bowl shaped with the maximum OH radical at the central region, where the local flow axial velocity is relatively low. The bowl shaped flame generated by the present burner is similar to the previously reported low swirl flames.^{2,3,28,29} Besides the bowl shape flame, the present

premixed flame exhibits different shapes due to the complex turbulent motions induced by various physical phenomena dominating the low swirl flow field. Previous investigations showed that large-scale motions instantaneously wrinkle the flame front and form a W-shaped flame.^{30–32} Present experimental investigations reveal that the same W-shaped flame can instantaneously appear at the central region of the swirling jet. Figure 3(d) shows that the off-central parts of the flame front propagate upstream through the low velocity regions initiated by hydrodynamic instabilities at the shear layers, while the central part of the flame is dragged further downstream by a high-velocity structure. Figure 3(e) shows that a recirculation zone (RZ) (white lines) exists downstream of the flame front. Such recirculation zone appears temporally at $Z/D > 1$. Figure 4 presents the ensemble averaged low swirl flow field using (a) simultaneous PIV and OH-PLIF and (b) OH* chemiluminescence. Results

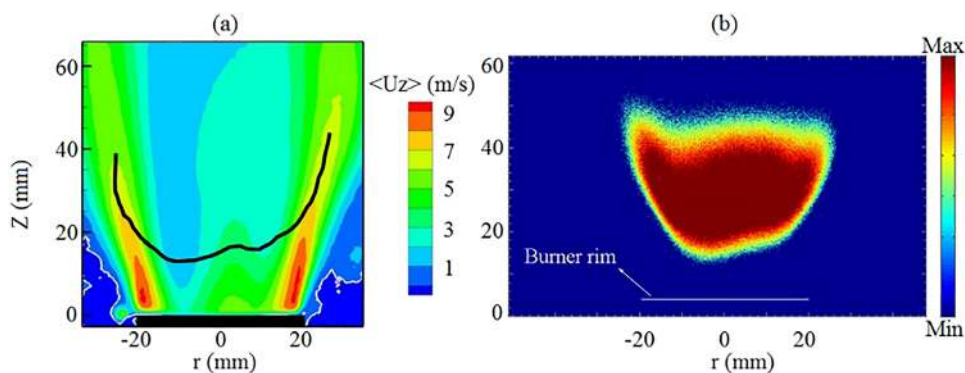


FIG. 4. Ensemble averaged low swirl flame features using (a) simultaneous axial velocity distribution from PIV and flame boundary (solid line) from OH-PLIF and (b) OH* chemiluminescence.

reveal that the overall shape of the low swirl flame is bowl shape and the ensemble averaged flow field is devoid of any recirculation zone. Previous numerical simulations of the reacting low swirl flow generated by the burner developed at Lund University showed the same temporal recirculation zone downstream of the flame front.³³

B. Low swirl flame under acoustic excitations

Low swirl burners are developed to be utilized in various combustion devices, namely, gas turbines, boilers and furnaces.^{4,22} However, thermoacoustic instability is one of the main issue of concern in low swirl combustion, since the low swirl flame is lifted and is highly prone to disturbances. Therefore, it is mandatory to study reacting low swirl flow dynamics in acoustically driven environments with various forcing frequencies and amplitudes. It is known that low or intermediate frequency thermoacoustic instabilities are highly important to make near lean blow out flames applicable in large combustion devices (e.g., boilers).³⁴ In this study, relatively low frequency acoustic waves are chosen to study effects of acoustic perturbation amplitude on lean premixed low swirl flame dynamics. The selected forcing frequencies are in the range of frequencies utilized in previous investigations.^{12,15} The objective of the present section is to address effects of the acoustic wave amplitude on low swirl flame and flow dynamics aim in understanding both linear and nonlinear responses of the flame to acoustic excitations. To such aim, it is necessary first to study effects of acoustic contents of the experimental setup on the acoustic waves generated by the loudspeaker to choose appropriate forcing frequencies (f_0) and amplitudes (A). In order to delineate effects of the settling chamber and contractions geometry (Fig. 1) on the generated acoustic waves, the wave equation for sound waves in a lossless medium is solved. To such aim, it is assumed that the pressure wave p' is a time harmonic wave as

$$p(\vec{x}, t) = p(\vec{x})e^{i\omega t}, \quad (1)$$

where $\omega = 2\pi f$ is the angular frequency. Using such assumptions, the three-dimensional wave equation yields the Helmholtz equation as follows:

$$\nabla \cdot \left(-\frac{1}{\rho} \nabla p \right) - \frac{\omega^2 p}{\rho c^2} = 0, \quad (2)$$

where ρ is density and c is speed of sound. The Helmholtz equation is solved using a finite element method using fourth order spectral elements. The computational domain is meshed using triangular elements. The maximum element size is set equal to $c/(60f_{\max})$. The inlet boundary condition is placed at the speaker outlet, through which incoming plane waves are imposed at various frequencies. Moreover, the inlet boundary condition also involves an outgoing radiating wave. The outlet boundary condition of the computational domain is placed at the burner outlet, which is prescribed by an outgoing radiating plane wave boundary condition. A sound hard boundary condition is used at walls.

Figure 5 plots outgoing acoustic power at the burner outlet normalized by the incoming acoustic power at the inlet boundary condition at various forcing frequencies. The incoming and outgoing acoustic powers are defined as follows:

$$\Gamma_{in} = \int \frac{p_0^2}{2\rho c} dA, \quad (3)$$

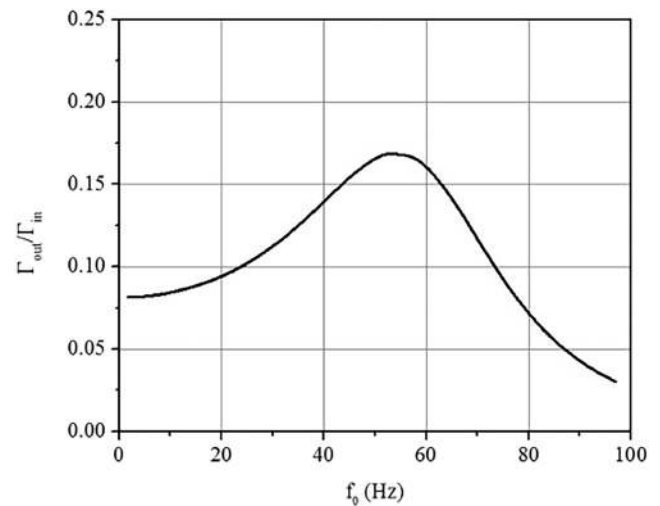


FIG. 5. Normalized acoustic power.

$$\Gamma_{out} = \int \frac{p^2}{2\rho c} dA, \quad (4)$$

where p_0 is the amplitude of the incoming pressure wave at the inlet boundary condition.

The result shows that the ratio of the acoustic power of the outgoing waves to the incoming waves is at the maximum value, when the experimental setup is forced by acoustic waves at forcing frequencies of $50 < f_0$ (Hz) < 57 . This finding indicates that, at such forcing frequencies, the maximum energy of the acoustic waves transmits through this experimental setup. However, the acoustic power decreases at the burner outlet as the forcing frequency increases. The same reduction in the acoustic power at the burner outlet occurs at very low forcing frequencies ($f_0 < 50$ Hz). Figure 5 reveals that the acoustic excitations at 50 Hz have the most vigorous effects on the low swirl flame. This finding collaborates the high speed OH* chemiluminescence imaging results presented in the following parts of the paper.

In the present study, investigations were carried out to select the acoustic wave characteristics in a way to achieve the desire forcing amplitudes at the burner outlet to study linear and nonlinear responses of the low swirl flame to the acoustic disturbance. However, investigations showed that adjusting the input voltage of the loudspeaker with the amplifier at a constant forcing frequency is not enough to generate acoustic waves with low to high amplitudes at the burner outlet. Therefore, instead of changing the input voltage of the loudspeaker to adjust the acoustic power, inspired by Fig. 5, the frequency of the acoustic wave is adjusted slightly to achieve the desired acoustic power to study effects of the acoustic excitation amplitude on the reacting low swirl flow dynamics. In the following parts of the paper forcing frequencies of 50, 65, 80 Hz, for which amplitude of the acoustic waves at the burner outlet is, respectively, high, medium, and low are chosen to study effects of acoustic excitations on the reacting low swirl flow dynamics. However, it is well known that amplitude of the loudspeaker response changes drastically below a specific frequency due to the resonance. Here, in order to make sure that loudspeaker response curve is flat at the

selected forcing frequencies, the loudspeaker is subjected to several tests to evaluate the speaker response at low forcing frequencies. To such aim, a pressure sensor was located at a fixed distance in front of the speaker. Then, sinusoidal waves were generated by the signal generator at low frequencies with constant amplitude. For the sake of brevity, such investigations are not presented here. Studies indicated that the acoustic wave amplitude is constant ($p'/p_{\text{Mean}} = 0.045\%$) at all forcing frequencies considered here. In another word, the loudspeaker response curve is flat at the selected forcing frequencies.

Based on Fig. 4(b), the length of the flame is approximately 34 mm. Accordingly, by considering the sound speed in the combusted methane/air mixture at equivalence ratio of 0.62 to be 823.3 m/s, the forcing acoustic wavelengths at forcing frequencies of 50, 65, and 80 Hz are respectively, 471, 362, and 294 times larger than the flame length. Therefore, all parts of the flame sense approximately the same pressure level at a single phase of the excitations. In the present paper, the velocity perturbations are measured using the hot wire located upstream of the swirler. The location of the hot wire is chosen to make sure that this intrusive measurement device has no effect on the flame and flow dynamics and to protect the instrument from flame flashback. Based on the burner dimensions and flame position [Fig. 4(b)], the axial distance between the hot-wire location and the flame front is 108 mm. Therefore, there is a phase difference between the recorded velocity fluctuations and the ones perturbing the flame. Considering the sound propagation speed in the fresh reactants to be 347.2 m/s, such phase differences are 9° , 7.3° , and 5.6° for the selected forcing frequencies of 80, 65, and 50 Hz, respectively, which are considered in the data postprocessing. It should be mentioned that the Helmholtz frequency of the present settling chamber is 26 Hz. Therefore, all the selected forcing frequencies (50, 65, and 80 Hz) are higher than the Helmholtz frequency, which means that there are acoustic waves (both standing and traveling) in the experimental setup at all the selected forcing frequencies.

Figure 6 plots time traces of heat release and velocity fluctuations of the excited low swirl flame at $f_0 = 50, 65, 80$ Hz during the acoustic excitations, acquired by high speed OH^* chemiluminescence imaging, and hot wire anemometry, respectively. Since the acoustic wave amplitude is high at the burner outlet in some cases, first, the experiments were performed for more than 60 s in each case to make sure that there is no transitioning regime in the data. Then, data are collected for 3 s to calculate ensemble averaged heat release and velocity and corresponding fluctuations. Here, heat release in each time instance is calculated by integrating OH^* signal through the whole field of the view in the chemiluminescence imaging. Then, this set of data is used to calculate mean heat release and heat release fluctuations. Finally, heat release and velocity fluctuations are normalized by the ensemble averaged heat release and velocity of the unexcited reacting low swirl flow, respectively. Furthermore, the flame lift-off distance from the burner rim measured using OH^* chemiluminescence data is also plotted in Fig. 6, which is normalized by the lift-off distance of the ensemble averaged unexcited flame. The flame lift-off distance is the minimum distance between the flame front and the burner outlet. Time traces of the velocity show that the amplitudes of the acoustic waves are approximately 50%, 20%, and 10% of the mean flow velocity at the forcing frequencies of 50, 65, and 80 Hz, respectively. These results collaborate the main findings of Fig. 5.

Figure 6 shows that both heat release fluctuations and the flame lift-off distance respond periodically to the sinusoidal velocity perturbations induced by the acoustic excitations at all selected forcing conditions. At low ($f = 80$ Hz and $A = 10\%$) and medium ($f = 65$ Hz and $A = 20\%$) forcing amplitudes, although the flame lift-off distance oscillates under acoustic excitations, the flame remains lifted during the excitations. Figure 6(a) shows that the low swirl flame flashes back into the burner at high amplitude excitations ($f = 50$ Hz and $A = 50\%$) at phase angles of 270° – 360° . However, since there is no optical access available inside the burner to discern the flame location, the negative value of the normalized flame lift-off

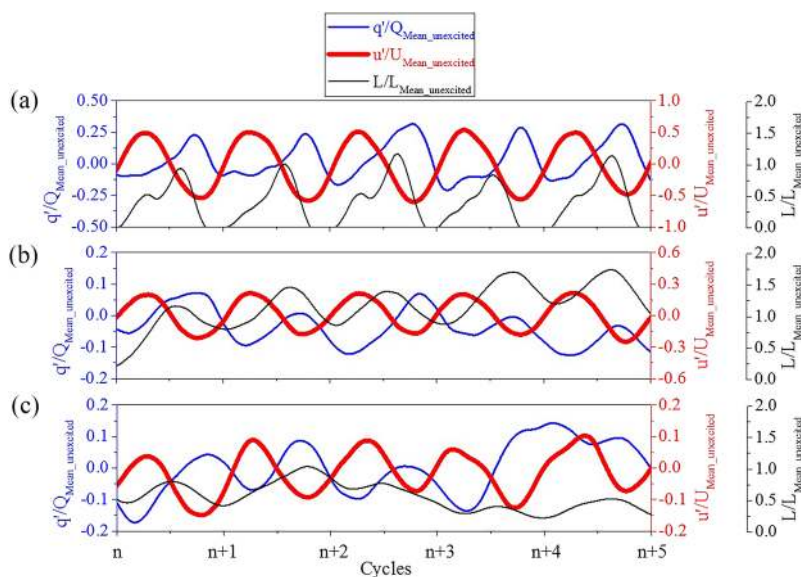


FIG. 6. Time traces of the normalized heat release and velocity fluctuations and the flame lift-off distance for the low swirl flame under (a) high amplitude ($A = 50\%$ and $f_0 = 50$ Hz), (b) medium amplitude ($A = 20\%$ $f_0 = 65$ Hz), and (c) low amplitude ($A = 10\%$ and $f_0 = 80$ Hz) acoustic excitations.

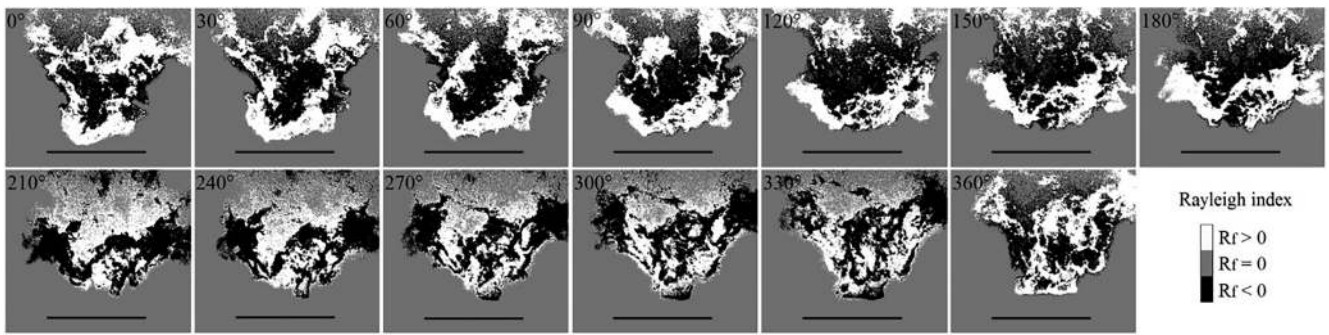


FIG. 7. Temporal OH* distribution of the low swirl flame under low amplitude acoustic excitations ($A = 10\%$) colored by the local Rayleigh index.

distance, which indicates the location of the flame inside the burner, is not shown in Fig. 6. Time traces of the flame lift-off distance also show that $L/L_{\text{Mean_unexcited}}$ is usually less than 1 in all the excited cases, which implies that the flame lift-off distance decreases under acoustic excitations.

Figure 6 also shows that phase differences between velocity fluctuations and heat release fluctuations and flame lift-off distance are not constant during the excitations. However, here, the ensemble averaged values of such phase differences are calculated using data over 150 cycles of the excitations. Results show that heat release fluctuations have 152° , 154° , and 186° phase differences with the velocity perturbations at the forcing frequencies of 50, 65, and 80 Hz, respectively. Furthermore, the phase differences between the lift-off distance and forcing acoustic waves are 102° , 103° , and 100° for the excited cases at 50, 65, and 80 Hz, respectively.

Figures 7 and 8 show evolution of the low swirl flame over one cycle of acoustic excitations at low and medium amplitudes excitations, respectively, using high speed OH* chemiluminescence imaging. The location of the burner rim is shown for the reference. In an attempt to quantify the thermoacoustic couplings, the flame is colored by local Rayleigh index, which is calculated using³⁵

$$R_f = \int_0^1 \frac{p'q'}{p_{\text{rms}}q} d\xi, \quad (5)$$

where p' is pressure fluctuation, q' is heat release fluctuation, p_{rms} is root mean square of pressure and q is mean heat release. The positive value of Rayleigh index indicates an acoustically driving region, where the energy feeds back to the acoustic perturbations, while the negative value shows an acoustically dampening region.

Figure 7 shows that the flame shape under low amplitude acoustic excitations is approximately bowl shape at all the forcing phases. However, the flame lift-off distance slightly changes under acoustic excitations. Spatial distribution of Rayleigh index shows that the thermoacoustic coupling is positive at the base of the flame at the phase angles of 0° – 90° . However, as the phase angle increases, the base of the flame experiences both acoustically dampening and driving processes. Further downstream of the flame base, the Rayleigh index is usually negative at the center of the flame at the phase angles of 0° – 180° . However, at the negative amplitude half of the acoustic perturbations the center of the flame experiences both dampening and driving processes. Results also indicate that Rayleigh index can be both negative and positive at the boundary of the flame at all the forcing phases.

Figure 8 shows that the flame shape is highly phase dependent under medium amplitude acoustic excitations. The lifted flame is bowl shaped at phase angle of 0° . As the excitation phase increases, the central parts of the flame gradually move downstream, while the off-central parts propagate upstream. Combination of these movements results in more flat type flame. Then, at the negative amplitude

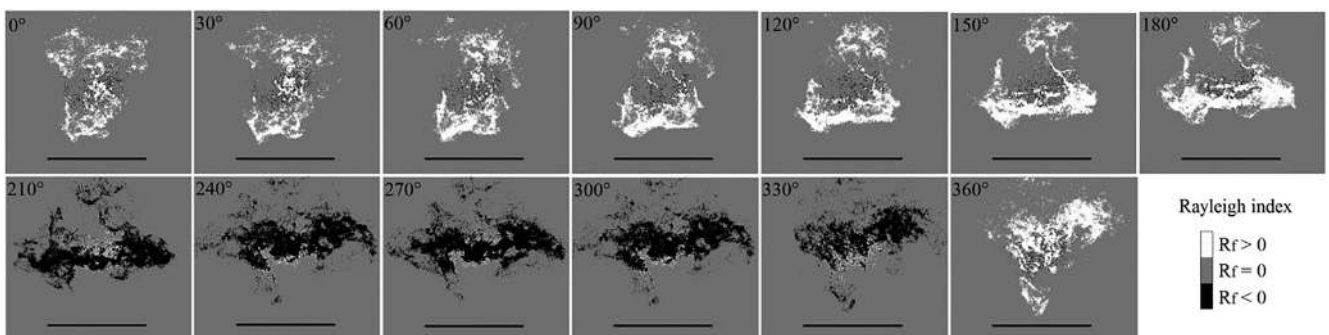


FIG. 8. Temporal OH* distribution of the low swirl flame under medium amplitude acoustic excitations ($A = 20\%$) colored by the local Rayleigh index.

half of the acoustic excitations, some parts of the flame propagate upstream from the central region, until the flame resumes its original bowl shape at the phase angle of 360° . Results also show that the low swirl flame is compact in the axial direction at phase angles of 150° – 300° , while it is dispersed at other phases. Spatial distribution of Rayleigh index shows that the acoustically driving mechanism occurs at the positive amplitude half of the acoustic excitations, while at the negative amplitude half of the perturbations almost whole parts of the flame act as a damping mechanism.

To get a better insight into the low swirl flame and flow responses to the acoustic excitations, Fig. 9 shows spatial distributions of instantaneous and ensemble averaged axial velocity and flame boundary using simultaneous PIV and OH-PLIF methods for the low swirl flame under the medium amplitude acoustic excitations. It should be mentioned that the instantaneous results are extracted from different cycles of the excitations. However, all acquired phase-locked data approximately show similar flow and flame features. Instantaneous results show that the annular swirling jet is more coherent at phase angles of 0° and 90° as compared to the phase angles of 180° and 270° , which indicates that the annular jet experiences more vigorous instabilities at the negative amplitude half of the harmonic excitations. Moreover, ensemble-averaged results show that the annular swirling jet has much higher velocity at the positive amplitude half of the harmonic excitations. Here, isolines of zero axial velocity (white lines) are used to discern boundaries of the recirculation zone and vortex structures. Comparison of Figs. 9 and 3 shows that the recirculation zone is stronger in the excited flame as compared to the unexcited low swirl flame. However, ensemble averaged phase-locked results [Fig. 9(b)] reveal that the recirculation zone diminishes at all phases except phase angle of 270° . Based on these results, external excitations induce much stronger recirculation zone downstream of the flame front as compared to the unexcited case. Such changes in the flow features alter the flame shape. Figure 9 shows that as the recirculation zone moves

downstream, the flame flattens. The flame movements observed in Fig. 8 are due to the existence of the temporal recirculation zone induced by the acoustic excitations. Present investigations show that unlike high swirl combustion in which recirculation zone has no direct effect on the flame response to the forcing,³⁶ recirculation zone dynamics under acoustic excitations play a significant role in inducing flame movements in low swirl combustion.

Figure 10 shows the flame evolution over a cycle of the high amplitude acoustic excitations ($A = 50\%$). The overall flame evolution and movements are similar to the excited case under medium amplitude acoustic excitations (Fig. 8). Figure 10 shows that the flame becomes completely flat type at phase angles of 30° – 90° . Then, as the phase angle increases, the flame gradually flashes back into the burner due to a similar temporal recirculation zone observed in Fig. 9. Finally, the flame propagates out of the burner at phase angles of $\theta > 0^\circ$ and reaches its original lifted state. Spatial distribution of Rayleigh index shows similar pattern as the one observed in the flame under medium amplitude excitations. Almost all parts of the flame act as a driving mechanism at the phase angles of 0° – 180° , while they act as a damping mechanism for the acoustic energy at phase angles of 180° – 360° . Comparison of Figs. 7, 8, and 10 reveals that, at each phase of the acoustic excitations, all parts of the flame experience a coherent thermoacoustic coupling pattern under medium and high forcing amplitudes, while at low forcing amplitudes various thermoacoustic coupling patterns occur in the flame. Obviously, all above coupling patterns are phase dependent.

Present study shows that acoustic excitations with high forcing amplitudes sometimes induce flame blowout. Figure 11 shows flame evolution over a cycle of the excitations prior to the flame blowout. Similar to the other excited cases (Figs. 8 and 10), the flame flattens at positive amplitude half of the excitations. Moreover, the flame breaks down into smaller segments as the phase angle increases. Figure 11 shows that the dispersed regions of heat release in the

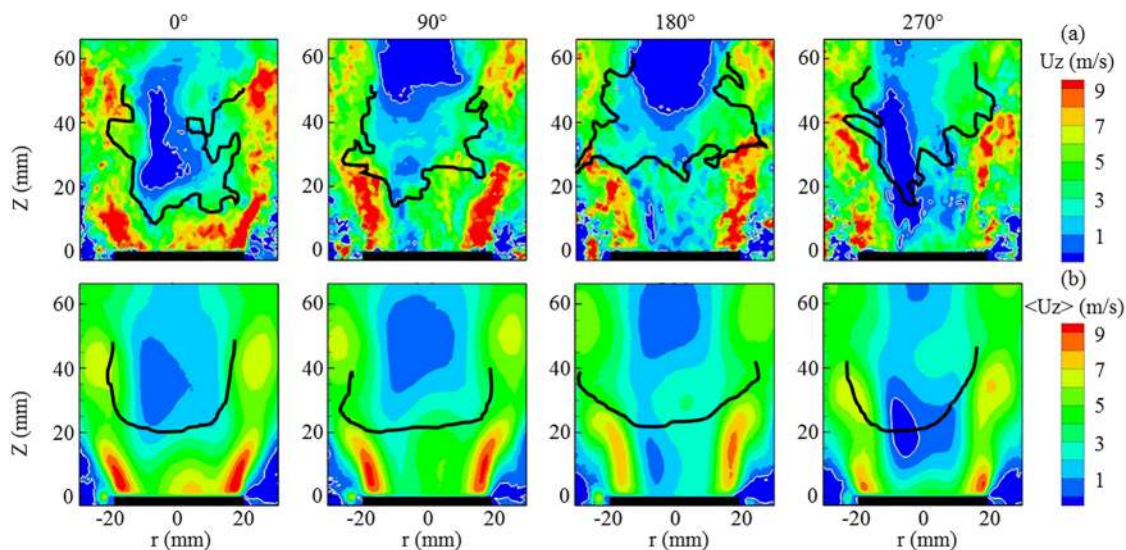


FIG. 9. (a) Instantaneous and (b) ensemble averaged axial velocity distributions and low swirl flame positions under medium amplitude acoustic excitations ($A = 20\%$).

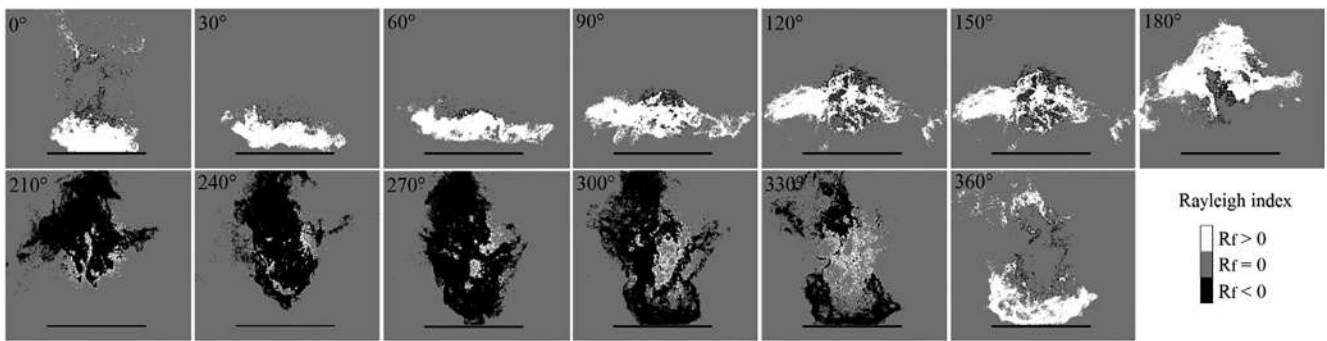


FIG. 10. Temporal OH* distribution of the low swirl flame under high amplitude acoustic excitations ($A = 50\%$) colored by the local Rayleigh index.

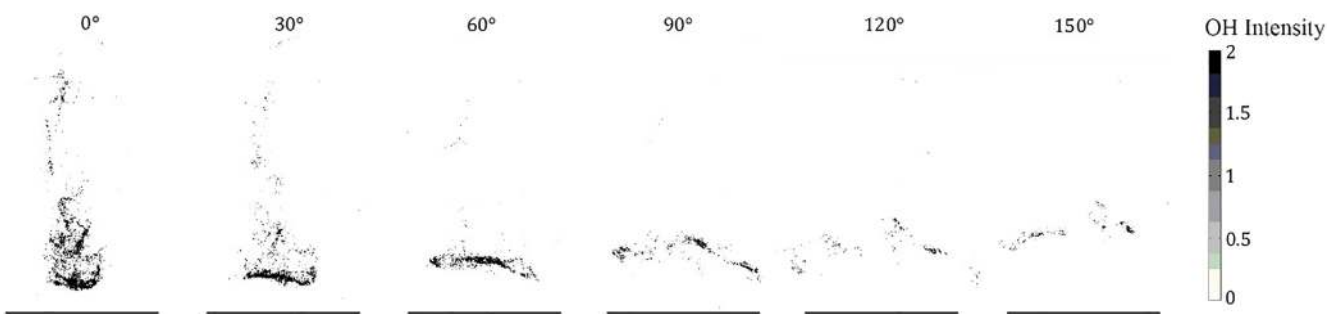


FIG. 11. Temporal OH* distribution of the low swirl flame under high amplitude acoustic excitations ($A = 50\%$, ended up in blowout) during the blowout.

excited flame cannot be reorganized to form the compact flame again as the phase angle increases. Therefore, the coupling of the acoustic excitations and the flame dynamics diminishes at such conditions. This is in contrast to the results presented in Fig. 10, in which the flat flame is reorganized to form the flashed back and then stable flames again. In order to explain the key parameter initiating the flame blowout, the excited low swirl dynamics are considered in the following parts of the paper.

Figure 12(a) plots normalized heat release fluctuations and the flame lift-off distance over the last 30 cycles of the excitations, before flame blowout, for the flame under high amplitude acoustic perturbations. The zoom-in data [highlighted region in Fig. 12(a)] during five cycles of excitations are also presented in Fig. 12(b) to show details of the response of the flame to the acoustic perturbations. Results show that the flame lift-off distance responds periodically to the acoustic excitations. Here, the averaged phase difference between

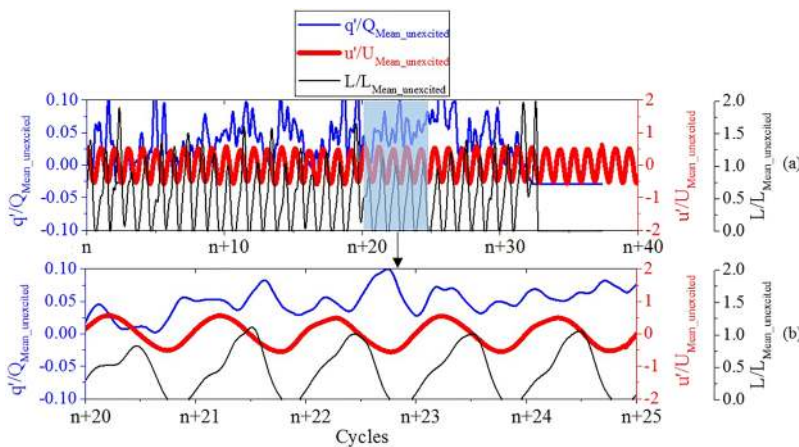


FIG. 12. Time traces of normalized heat release and velocity fluctuations and the flame lift-off distance for the low swirl flame under high amplitude acoustic excitations ($A = 50\%$, ended up in blowout).

the lift-off distance and forcing acoustic waves is 85° . Such phase difference is smaller than the corresponding phase difference in the flame under high amplitude acoustic excitations, which is not ended up in blowout.

Figure 12 also shows that heat release fluctuations do not respond periodically to the acoustic excitations prior to blowout, while, as it is already shown in Fig. 6, for the excited cases without flame blowout, the trends are periodic. These findings show that heat release responds aperiodic to the sinusoidal acoustic excitations prior to the flame blowout, while the overall flame movement is sinusoidal. Therefore, the precursor event of the flame blowout induced by the acoustic excitations consists of aperiodic heat release fluctuations.

Although heat release fluctuations show aperiodic features under high amplitude acoustic excitations, prior to the flame blowout, there are deterministic features in the results. In an attempt to find such features, Figs. 13(a) and 13(b) plot power spectra of acoustic velocity and heat release fluctuations for the excited cases. To such aim, velocity data are extracted upstream of the swirler using the hot wire. Furthermore, using OH^* chemiluminescence images, heat release fluctuations are calculated by integrating OH^* intensity throughout the images. Here, the frequency and power are normalized by the forcing frequency and maximum power in each case, respectively. Power spectra of the velocity fluctuations show that there is a higher harmonic mode of $2f_0$ in the FFT of velocity fluctuation data for the flame under high amplitude excitations ($A = 50\%$). However, power of such harmonic is much lower than the power of the forcing wave (f_0). Power spectrum of heat release

fluctuations of the flame under high amplitude acoustic excitations ($A = 50\%$) shows that the harmonic in velocity fluctuations induces a much stronger harmonic in heat release fluctuations. The same phenomenon can be observed in power spectrum of heat release fluctuations of the flame under high amplitude acoustic excitations, which ended up in flame blowout ($A = 50\%$ - Blowout). Results indicate that acoustic excitations at the high amplitude condition induce heat release fluctuations with dominant frequencies of f_0 , $1.14f_0$, $2f_0$, and $3f_0$ Hz. Interestingly, heat release fluctuations are stronger at $2f_0$ as compared to f_0 . High amplitude acoustic excitations induce nonlinear features in flame dynamics, which lead to amplification of higher harmonics in heat release fluctuations.

In order to further characterize dynamics of the low swirl flame under acoustic excitations, time-delay embedded theorem proposed by Takens³⁷ is used here to study heat release fluctuations in the higher dimensional phase space. To such aim, the optimum value of time delay ($\tau = 1.4$ ms) and minimum value of embedding dimension ($d = 7$) utilized in the model are calculated based on average mutual information³⁸ and method of false nearest neighbors,³⁹ respectively. Figure 13(c) shows the reconstructed phase portraits of heat release fluctuations for the excited low swirl flames. Obtained results show that the phase portraits are more regular and have oval (or ear) shape for the flame under high amplitude acoustic excitations ($A = 50\%$). Reducing the forcing amplitude to 20% or 10% results in more scattered oval feature. Such scattered trajectories in the excited cases with $A = 10\%$ or 20% are due to the variations of heat release fluctuation amplitude during various cycles of the excitations. These findings are in-line with previous

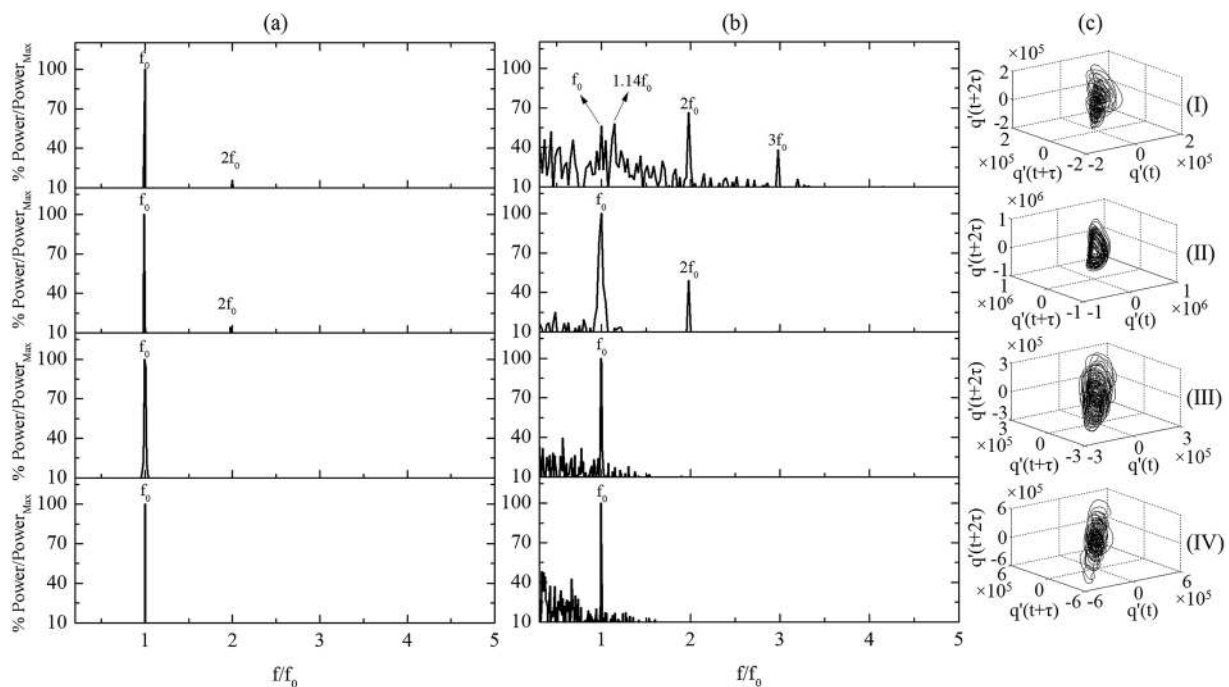


FIG. 13. (a) Power spectrum of acoustic velocity, (b) power spectrum of heat release fluctuations, and (c) the reconstructed phase portraits of the global heat release fluctuations for low swirl flame under acoustic excitations with forcing amplitudes of (I) $A = 50\%$ (flame ended up in blowout), (II) $A = 50\%$, (III) $A = 20\%$ and (IV) $A = 10\%$.

investigations of Pawar *et al.* on reacting wakes by showing that increasing the forcing amplitude results in more deterministic features in heat release fluctuations.⁴⁰ However, further increases of the forcing amplitude result in similar scattered patterns as the one observed in the flame under low amplitude acoustic perturbations. The scatter of the trajectory in this case is due to other frequency contents of the heat release fluctuations, especially the rich harmonic contents observed in Fig. 13(b), induced by nonlinearities generated by the high amplitude acoustic excitations.

Flame blowout can be a symptom of such nonlinearity. This physical phenomenon is somewhat analogous to the energy transfer in turbulent flows. It is well known that as the kinetic energy of a turbulent flow increases, energy is transferred from large scale structures to the small scale structures. In the present case, high amplitude acoustic excitations transfer a large amount of the acoustic energy to the turbulent reacting flow. In such conditions, it seems that the combustion field cannot handle the energy. Therefore, a noticeable amount of the energy is transferred to the higher harmonics of the perturbations. In this way, the combustion flow field can handle the energy by transferring the acoustic energy to the higher modes of the heat release fluctuations. As a result, the flame responds aperiodic to the excitations, which finally results in incapability of the flame to reorganize itself from the dispersed flame (Fig. 11), which is followed by the flame blowout. Figure 13 also shows that heat release fluctuations respond linearly to the acoustic excitations at low ($A = 10\%$) and medium amplitude ($A = 20\%$) conditions.

IV. CONCLUSIONS

Low swirl stabilization is a novel dry low NO_x mode to stabilize lean premixed flames. However, this combustion mode is highly prone to acoustic perturbations, since the premixed flame stabilized by the low swirl flow is lifted and detached from the burner. The main objective of the present investigation is to utilize simultaneous PIV and OH-PLIF methods along with OH* chemiluminescence and hot-wire measurements to evaluate key effects of acoustic perturbations on a lean premixed low swirl flame.

Low swirl flame response to low to intermediate amplitude acoustic perturbations showed that both heat release fluctuations and the flame lift-off distance respond periodically to the acoustic perturbations. As the forcing amplitude increases, the flame lift-off distance changes drastically insofar as the flame flashes back or blows out during the excitations. Such drastic flame movements are due to a relatively strong recirculation zone induced by acoustic excitations. Phase portraits results showed that increasing the acoustic wave amplitude results in more deterministic features in the flame response, if the flame does not blowout due to the excitations. The data obtained prior to the flame blowout showed that the heat release fluctuations have a highly nondeterministic aperiodic response to the perturbations, while the flame lift-off distance responds periodically to the perturbations. The present investigations showed that high amplitude acoustic excitations induce nonlinear features in the flame dynamics, which lead to amplification of higher harmonics in heat release fluctuations. Flame blowout can be a symptom of such nonlinearity.

In an attempt to further study the low swirl flame dynamics under acoustic excitations, the Rayleigh index was calculated at

various phases of the acoustic excitations. Obtained results revealed that, at low amplitude acoustic excitations, the base of the flame acts as an acoustically driving region at the phase angles of 0° – 90° , while at such phase angles, the damping process occurs at the center of the flame. However, as the phase angle increases, the center and base of the flame experiences both damping and driving processes. Results also showed that the boundary of the flame experiences both damping and driving processes at all phases of the low amplitude acoustic excitations. However, at medium and high amplitude acoustic excitations, the acoustically driving mechanism occurs through almost the whole flame regions at the positive amplitude half of the acoustic perturbations, while at the negative amplitude half of the perturbations, almost all parts of the flame act as a damper for the acoustic energy.

ACKNOWLEDGMENTS

The current investigations have been carried out at the National Center for Combustion Research and Development (NCCRD), Indian Institute of Technology Madras (IITM).

REFERENCES

- 1S. M. Correa, "Review of NO_x formation under gas turbine conditions," *Combust. Sci. Technol.* **87**, 329–362 (1993).
- 2R. K. Cheng, "Velocity and scalar characteristics of premixed turbulent flames stabilized by weak swirl," *Combust. Flame* **101**, 1–14 (1995).
- 3D. T. Yegian and R. K. Cheng, "Development of a lean premixed low-swirl burner for low NO_x practical applications," *Combust. Sci. Technol.* **139**, 207–227 (1998).
- 4M. R. Johnson, D. Littlejohn, W. A. Nazeer, K. O. Smith, and R. K. Cheng, "A comparison of the flow fields and emissions of high-swirl injectors and low-swirl injectors for lean premixed gas turbines," *Proc. Combust. Inst.* **30**, 2867–2874 (2005).
- 5T. Lieuwen, H. Torres, C. Johnson, and B. T. Zinn, "A mechanism of combustion instability in lean premixed gas turbine combustors," *J. Eng. Gas Turbines Power* **123**, 182–189 (2001).
- 6M. Bauerheim, F. Nicoud, and T. Poinsot, "Progress in analytical methods to predict and control azimuthal combustion instability modes in annular chambers," *Phys. Fluids* **28**, 021303-1–021303-27 (2016).
- 7V. V. Pulikkottil and R. I. Sujith, "Acoustic-hydrodynamic-flame coupling—a new perspective for zero and low Mach number flows," *Phys. Fluids* **29**, 046102-1–046102-7 (2017).
- 8S. R. Chakravarthy, R. Sampath, and V. Ramanan, "Dynamics and diagnostics of flame-acoustic interactions: A review," *Combust. Sci. Technol.* **189**, 395–437 (2017).
- 9B. Zhang, M. Shahsavari, Z. Rao, S. Yang, and B. Wang, "Contributions of hydrodynamic features of a swirling flow to thermoacoustic instabilities in a lean premixed swirl stabilized combustor," *Phys. Fluids* **31**, 075106-1–075106-11 (2019).
- 10M. Shahsavari, I. B. Aravind, S. R. Chakravarthy, and M. Farshchi, "Experimental study of lean premixed low swirl flame under acoustic excitations," in *International Symposium: Thermoacoustic Instabilities in Gas Turbines and Rocket Engines: Industry Meets Academia*, 2016, paper GTRE 029.
- 11D. Durox, T. Schuller, and S. Candel, "Combustion dynamics of inverted conical flames," *Proc. Combust. Inst.* **30**, 1717–1724 (2005).
- 12D. M. Kang, F. E. C. Culick, and A. Ratner, "Combustion dynamics of a low-swirl combustor," *Combust. Flame* **151**, 412–425 (2007).
- 13Y. Huang and A. Ratner, "Experimental investigation of thermoacoustic coupling for low-swirl lean premixed flames," *J. Propul. Power* **25**, 365–373 (2009).
- 14M. Shahsavari, M. Farshchi, B. Wang, and D. Zhao, "Response of a low swirl premixed flame to acoustic perturbations," in *27th International Colloquium on the Dynamics of Explosions and Reactive Systems*, 2019, paper 143.

- ¹⁵I. Yilmaz, A. Ratner, M. Ilbas, and Y. Huang, "Experimental investigation of thermoacoustic coupling using blended hydrogen-methane fuels in a low swirl burner," *Int. J. Hydrogen Energy* **35**, 329–336 (2010).
- ¹⁶D. W. Davis, P. L. Therkelsen, D. Littlejohn, and R. K. Cheng, "Effects of Hydrogen on the thermo-acoustics coupling mechanisms of low-swirl injector flames in a model gas turbine combustor," *Proc. Combust. Inst.* **34**, 3135–3143 (2013).
- ¹⁷J. Ranalli and D. Ferguson, "Measurement of flame frequency response functions under exhaust gas recirculation conditions," *J. Eng. Gas Turbines Power* **134**, 091502 (2012).
- ¹⁸J. Zhang and A. Ratner, "Effect of pressure variation on acoustically perturbed swirling flames," *Proc. Combust. Inst.* **36**, 3881–3888 (2017).
- ¹⁹N. Bagheri-Sadeghi, M. Shahsavari, and M. Farshchi, "Experimental characterization of response of lean premixed low-swirl flames to acoustic excitations," *Int. J. Spray Combust. Dyn.* **5**, 309–328 (2013).
- ²⁰M. Shahsavari and M. Farshchi, "Large eddy simulation of low swirl flames under external flow excitations," *Flow, Turbul. Combust.* **100**, 249–269 (2018).
- ²¹R. K. Cheng and H. Levinsky, "Lean premixed burners," in *Lean Combustion*, edited by D. Dunn-Rankin (Academic Press, 2008), pp. 161–177.
- ²²R. K. Cheng, D. T. Yegian, M. M. Miyasato, G. S. Samuelsen, C. E. Benson, R. Pellizzari, and P. Loftus, "Scaling and development of low-swirl burners for low emission furnaces and boilers," *Proc. Combust. Inst.* **28**(1), 1305–1313 (2000).
- ²³R. Mei, "Flow due to an oscillating sphere and an expression for unsteady drag on the sphere at finite Reynolds number," *J. Fluid Mech.* **270**, 133–174 (1994).
- ²⁴A. Melling, "Tracer particle and seeding for particle image velocimetry," *Meas. Sci. Technol.* **8**, 1406–1416 (1997).
- ²⁵C. Tropea, A. L. Yarin, and J. F. Foss, *Springer Handbook of Experimental Fluid Mechanics* (Springer, 2007).
- ²⁶R. Santhosh and S. Basu, "Transient and blowoff of unconfined non-reacting swirling flame," *Combust. Flame* **164**, 35–52 (2016).
- ²⁷A. K. Prasad, R. J. Adrian, C. C. Landreth, and P. W. Offutt, "Effect of resolution on the speed and accuracy of particle image velocimetry interrogation," *Exp. Fluids* **13**, 105–116 (1992).
- ²⁸R. K. Cheng, D. Littlejohn, W. A. Nazeer, and K. O. Smith, "Laboratory studies of the flow field characteristics of low swirl injectors for adaptation to fuel-flexible turbines," *J. Eng. Gas Turbines Power* **130**, 021501 (2008).
- ²⁹D. Littlejohn, R. K. Cheng, D. Noble, and T. Lieuwen, "Laboratory investigations of low-swirl injectors operating with syngases," *J. Eng. Gas Turbines Power* **132**, 011502 (2010).
- ³⁰K. J. Nogenmyr, P. Petersson, X. S. Bai, A. Nauert, J. Olofsson, C. Brackman, H. Seyfried, J. Zetterberg, Z. S. Li, M. Richter, A. Dreizler, M. Linne, and M. Alden, "Large eddy simulation and experiments of stratified lean premixed methane/air turbulent flames," *Proc. Combust. Inst.* **31**, 1467–1475 (2007).
- ³¹K. J. Nogenmyr, P. Petersson, X. S. Bai, C. Fureby, R. Collin, A. Lantz, M. Linne, and M. Alden, "Structure and stabilization mechanism of a stratified premixed low swirl flame," *Proc. Combust. Inst.* **33**, 1567–1574 (2011).
- ³²K. J. Nogenmyr, C. Fureby, X. S. Bai, P. Petersson, R. Collin, and M. Linne, "Large eddy simulation and laser diagnostic studies on a low swirl stratified premixed flame," *Combust. Flame* **156**, 25–36 (2009).
- ³³M. Shahsavari, M. Farshchi, and M. H. Arabnejad, "Large Eddy simulations of unconfined non-reacting and reacting turbulent low swirl jets," *Flow, Turbul. Combust.* **98**, 817–840 (2017).
- ³⁴T. C. Lieuwen and V. Yang, *Combustion Instabilities in Gas Turbine Engines: Operational Experience, Fundamental Mechanisms, and Modeling* (American Institute of Aeronautics and Astronautics, 2005).
- ³⁵W. Pun, S. L. Palm, and F. E. C. Culick, "Combustion dynamics of an acoustically forced flame," *Combust. Sci. Technol.* **175**, 499–521 (2003).
- ³⁶J. O'Connor and T. Lieuwen, "Recirculation zone dynamics of a transversely excited swirl flow and flame," *Phys. Fluids* **24**, 075107-1–075107-30 (2012).
- ³⁷F. Takens, "Detecting strange attractors in turbulence, dynamical systems and turbulence," *Lect. Notes Math.* **898**, 366–381 (1981).
- ³⁸A. M. Fraser and H. L. Swinney, "Independent coordinates for strange attractors from mutual information," *Phys. Rev. A* **33**, 1134–1140 (1986).
- ³⁹M. B. Kennel, R. Brown, and H. D. Abarbanel, "Determining minimum embedding dimension using a geometrical construction," *Phys. Rev. A* **45**, 3403–3411 (1992).
- ⁴⁰S. A. Pawar, R. I. Sujith, B. Emerson, and T. Lieuwen, "Characterization of forced response of density stratified reacting wake," *Chaos* **28**, 023108 (2018).